ENGINEERING

# Four-dimensional micro-building blocks

T.-Y. Huang[1]*, H.-W. Huang[2,3]*, D. D. Jin[1,4]*, Q. Y. Chen[1,5], J. Y. Huang[1], L. Zhang[4,6], H. L. Duan[1,5]†



**Four-dimensional (4D) printing relies on multimaterial printing, reinforcement patterns, or micro/nanofibrous additives as programmable tools to achieve desired shape reconfigurations. However, existing programming approaches still follow the so-called origami design principle to generate reconfigurable structures by self-folding stacked 2D materials, particularly at small scales. Here, we propose a programmable modular design that directly constructs 3D reconfigurable microstructures capable of sophisticated 3D-to-3D shape transformations by assembling 4D micro-building blocks. 4D direct laser writing is used to print two-photon polymerizable, stimuli-responsive hydrogels to construct building blocks at micrometer scales. Denavit-Hartenberg (DH) parameters, used to define robotic arm kinematics, are introduced as guidelines for how to assemble the micro-building blocks and plan the 3D motion of assembled chain blocks. Last, a 3D-printed microscaled transformer capable of changing its shape from a race car to a humanoid robot is devised and fabricated using the DH parameters to guide the motion of various assembled compartments.**

## INTRODUCTION

Shape-morphing systems have been developed and used in broad areas, including camouflage (*1*), soft robotic actuators (*2*–*5*), solar tracking systems (*6*), and biomedical devices (*7*–*10*), to facilitate control and perception in the interactions between machines and their environments. Self-shaping from two-dimensional (2D) materials has the standard paradigm when constructing 3D morphing machines through computational origami designs. Self-shaping is a particularly unique and powerful technique when constructing small-scale machines, as it does not rely on a manual assembly process and the shape change can be actuated wirelessly (*11*–*17*). Researchers have also implemented programmable shape transformations in 2D materials by introducing fibrous micro- and nanoarchitectures (*18*, *19*), reinforcing nanoparticles (*20*–*23*), or inhomogeneous cross-linking (*24*, *25*) into stimuli-responsive gels or shape memory polymers. Although origami can mostly map any 3D shapes to intricate 2D blueprints, it renders the origami machines either poor load-bearing structures or resilient soft structures with limited load capability (*26*–*29*).

Recent advances in 3D printing have endowed directly printed machines with spatially controlled mechanical properties (*30*–*34*). Sophisticated multimaterial printing techniques that combine stimuli-responsive materials with various properties and micro/nano additives have been developed to enable programmable shape shifting in 3D printing (*35*, *36*). However, existing programming approaches are inherited directly from their origami counterparts. Thus, state-of-the-art 3D morphing machines are still generated through 3D printing in planar 2D self-folding structures (*37*, *38*). The lack of a programmable design paradigm that is specific to 3D printing can be attributed to the notably increased computational complexity of the forward and inverse designs of 3D-to-3D shape transformations. Moreover, the finite element analysis (FEA) (*39*, *40*), which has long been the only tool able to simulate shape transformations of direct 3D-printed structures, is a time-consuming process, especially when analyzing the evolution of a complex 3D shape. The computational load considerably increases as programmable designs become more complex. Modular designs as an alternative have been investigated in reconfigurable robotics for decades to enrich the morphologies, capabilities, and degrees of motion in single robots (*41*–*43*). Several algorithms have been developed for automatically generating the design assembly and motion planning in modular robots (*44*). However, modular design algorithms can hardly be applied to small-scale machines because of fundamental differences in the design, fabrication, and actuation principles.

In this work, we propose a programmable morphing modular design, inspired by modular robotics (*41*–*44*) and LEGO-like building blocks (*45*), to facilitate the design of complex 3D-to-3D shape transformations in direct 3D-printed microstructures. 4D direct laser writing (4D DLW) with submicrometer resolution (*46*) is used to construct a variety of microscaled shape-morphing building blocks using a two-photon polymerizable gel precursor whose cross-linking degree can be modulated by the laser dosage (Fig. 1A). Spatially and temporally controlled laser writing creates differentially cross-linked polymer networks that are vital to engineering the direction and magnitude of the shape transformation in response to external stimuli, thus endowing the building blocks with actively deforming layers, rigid layers, and compliant hinge joints. The modular design can reconstruct large and complex continuum shape transformations by assembling tiny replicated building blocks with small and simple discretized deformations. Each building block can be viewed as a motor with constrained rotation such that the assembly of the building blocks resembles a robotic arm whose movement can be captured by forward kinematics using Denavit-Hartenberg (DH) parameters. The DH parameters also provide us with guidelines for how to assemble the building blocks in 3D and plan their 3D motion. FEA is introduced to study the deformation of each kind of the replicated building blocks quantitatively. This analysis agrees well with the experimental results. Once we gain control of single building blocks through FEA, the DH parameters are used as the design guidelines

[1]State Key Laboratory for Turbulence and Complex Systems, Department of Mechanics and Engineering Science, BIC-ESAT, College of Engineering, Peking University, 100871 Beijing, People's Republic of China. [2]Koch Institute for Integrative Cancer Research, Massachusetts Institute of Technology, Cambridge, MA 02139, USA. [3]Division of Gastroenterology, Brigham and Women's Hospital, Harvard Medical School, Boston, MA 02115, USA. [4]Department of Mechanical and Automation Engineering, The Chinese University of Hong Kong, Shatin NT, Hong Kong, China. [5]CAPT, HEDPS and IFSA Collaborative Innovation Center of MoE, Peking University, 100871 Beijing, People's Republic of China. [6]Chow Yuk Ho Technology Centre for Innovative Medicine, The Chinese University of Hong Kong, Shatin NT, Hong Kong, China.
*These authors contributed equally to this work.
†Corresponding author. Email: hlduan@pku.edu.cn

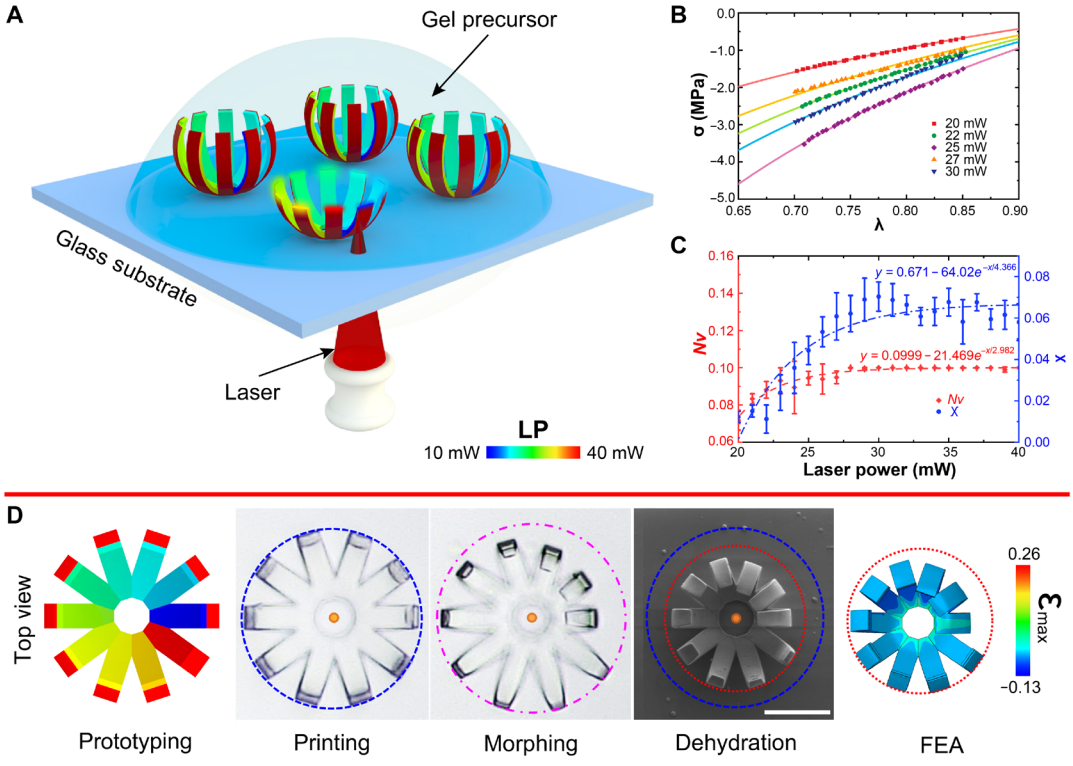


**Fig. 1. Spatial and temporal control in direct laser writing to enable spatially controlled differentially cross-linked polymer networks.** (**A**) Schematic of the printing process using a DLW system. The color bar of the laser power (LP) ranges from 10 to 40 mW. (**B**) Mechanical characteristics of the printed material with varying laser power, in which σ denotes the nominal compression stress and λ is the corresponding stretch ratio. (**C**) Effect of laser power on the cross-linking density $Nv$ and the Flory interaction parameter (χ). (**D**) Flower-like microstructure with programmed responsiveness to demonstrate controllable deformation. The outer (passive) layers of all petals were printed with a laser power of 40 mW and at a scanning speed of 8 mm/s; the inner (active) layer of each petal was printed at the same speed but with gradually increased laser power. After complete dehydration, the transformed petals exhibited the same bending curvature as those predicted by FEA. Scale bar, 40 μm.

to assemble various building blocks and program the 3D motion of each assembled compartments to enable complex 3D-to-3D transformations, thus notably reducing the computational load.

## RESULTS AND DISCUSSION

### FEA for the 4D micro-building blocks

Unlike 3D printing, 4D printing relies largely on mathematics to deal with sophisticated forward and inverse problems. The success of 4D printing depends on how accurate the computational models are in comparison to experimental results. Typically, accurate FEA incurs a heavy computational load, and divergence becomes a critical issue when the simulated 3D model becomes more complicated. To address this issue, we propose a modular design in which a large and complicated 3D structure and its shape transformation can be reconstructed by using small and discretized building blocks. These building blocks follow DH parameters that define the forward and inverse kinematics of assembled chain blocks. FEA is then introduced to study the deformation of each replicated building block.

Here, we carry out FEA on the basis of the Flory theory (*47*) in which we only need to characterize the mechanical properties of the gel polymerized with various laser powers at the fully swollen state. Other material properties, such as the cross-linking density and the Flory interaction parameter, along with the shape evolution with varying environmental conditions, can be subsequently obtained by the Flory theory. We first characterize the stress and strain relationship of the polymerized gels as functions of laser power via a group of in situ micromechanical compression tests (see section S1 and fig. S1). This test was conducted in an alkaline solution with pH ≈ 9 in which the samples were fully swollen. Figure 1B shows the dependence of the nominal compression stress on the stretch ratio of the gel samples with various photocuring parameters. The slopes of the fitted curves are directly associated with the laser powers adopted during photopolymerization. Following the work of Hong *et al.* (*47*), the nominal stress can be expressed by a partial derivative of the Legendre transformation–amended free-energy function concerning the deformation gradient, which yields the following (see sections S2 and S3 for more details)

$$\frac{\nu\sigma_{ij}}{kT} = Nv(F_{ij} - H_{ij}) + \left[J\ln\left(1-\frac{1}{J}\right) + 1 + \frac{\chi}{J} - \frac{\mu}{kT}J\right]H_{ij} \quad (1)$$

where $\sigma_{ij}$ is the nominal stress; $F_{ij}$ represents the deformation gradient; $J = \det F = \lambda_1\lambda_2\lambda_3 = 1 + \nu C$ is the invariant of the deformation gradient, where $\lambda_1$, $\lambda_2$, and $\lambda_3$ denote the polymer stretch in three principal directions, respectively; $C$ is the concentration of solvent molecules; $\nu$ is the volume per molecule; μ is the chemical potential; and $H_{ij}$ represents the inverse transpose of the deformation gradient. Here, χ is the Flory interaction parameter, denoting the extent of mixing between the solvent and polymer, which is a quantity dependent on the temperature and polymer concentration. To eliminate the singularity of the free energy in Eq. 1, we assign a free-swelling state rather than a dry state as a reference. Thus, we may reasonably

assume the chemical potential (μ) of the solvent to be zero, and Eq. 1 can be deduced as

$$Nv\left(\lambda_0\lambda_1' - \frac{1}{\lambda_0\lambda_1'}\right) + \lambda_0^2\lambda_2'^2\ln\left(1 - \frac{1}{\lambda_0^3\lambda_1'\lambda_2'}\right) + \frac{1}{\lambda_0\lambda_1'} + \frac{Nv(\lambda_0^2 - 1) + \lambda_0^3\ln\left(1 - \frac{1}{\lambda_0^3}\right) + 1}{\lambda_0^4\lambda_1'^2\lambda_2'^2} = \frac{\lambda_0^2\sigma'}{M} \quad (2)$$

with $M = kT/v$ and $\lambda_2'^2 = \lambda_1'^2 - \sigma'\lambda_0\lambda_1'/MNv$, where $\lambda_0$ is the stretch caused by free swelling. For a free-swelling isotropic deformation, we have $\lambda_1 = \lambda_2 = \lambda_3 = \lambda_0$. Equation 2 presents the inherent relationship between nominal stress and stretch, where the variables $\sigma'$ and $\lambda_1'$ can be determined experimentally from a uniaxial compression test (Fig. 1B). Subsequently, we set the product of $N$ and $v$ as a dimensionless parameter $Nv$, which characterizes the cross-linking density of the gel. We find that there are only two unknown parameters, $Nv$ and $\lambda_0$, in Eq. 2, whose values under different curing parameters can be evaluated by fitting Eq. 2 with the experimental data obtained from the uniaxial compression tests. Figure 1C presents the dimensionless parameter $Nv$ and the Flory interaction parameter $\chi$ as functions of laser power varying from 20 to 40 mW with a constant scanning speed. $Nv$ increases steadily and gradually reaches a plateau as the laser power approaches ~30 mW, which indicates that the gel is fully polymerized and that its cross-linking density eventually becomes constant. Similarly, the Flory interaction parameter $\chi$ gradually increases with an increase in laser power and becomes invariant when the laser power exceeds 30 mW. This further implies that the mixing interaction between the solvent and polymer gradually becomes stable.

After obtaining the material characterizations, we conducted a finite element simulation based on the commercial software Abaqus (Abaqus/CAE 2016, Dassault Systèmes S.A., France) to predict the shape evolution of the 3D-printed structures with varying chemical potential. We used Eq. 1 to describe the deformation of the gels in solvents with different chemical potentials. $Nv$ and $\chi$ with different laser power were imported into the simulation to determine the mechanical properties of the gels. To verify the accuracy of our finite element prediction of the shape morphing of the printed structures, a microflower composed of 10 bilayer-like petals (Fig. 1D), in which each was encoded with different laser dosages to enable different morphing curvatures, was engineered and tested in various environments to swell and shrink. The printed structure remained unchanged during swelling in the alkaline solution, although it shrank considerably in the acidic solution. Therefore, shrinking in an acidic solution is the dominant driving force used in this work to enable deformation of printed building blocks. In addition, the proposed FEA can even capture the shape when it is entirely dehydrated in air (Fig. 1D). In the following sections, we focus on the deformation of printed structures that are driven by shrinkage when decreasing the environmental pH values.

## Strategies for designing building blocks

Imagine that an arbitrary 3D structure is represented as a modular design constructed by the assembly of multiple replicated 3D-printed LEGO-like building blocks. Following this concept, we can represent a reconfigurable architecture as a modular morphing system consisting of various deformable 4D building blocks (Fig. 2A). The 4D building blocks can be simply viewed as a cubic cell with a bilayer configuration, including an active and a passive material. The heterobilayer configuration bends in the direction of the active layer as the active material shrinks. To further improve the deformability and programmability of the 4D building blocks, we introduce an articulated mechanism based on the ultrahigh precision heterogeneity of the 4D DLW. The articulated micro-building blocks consist of multiple thin bilayers composed of an active and a passive layer, compliant hinges, and rigid supports in a single building block. The compliant joints facilitate the deformation driven by the active layers and extend the degrees of morphing freedom. Figure 2B shows the calculated bending curvature of conventional 4D building blocks and the articulated 4D micro-building blocks with varying thickness ratio ($m$) between their active and passive layers. The bending curvature of the articulated one is at least two times larger than that of the conventional one (see section S3). Figure 2C also shows that the bending curvature of the articulated micro-building blocks can be fine-tuned by varying their slenderness ratio ($b$, width to height) and the laser power on the active layer (figs. S2 and S3). Owing to the spatially and temporally controlled cross-linking density in the printed material, the degrees of morphing freedom of the articulated building blocks can be further extended by varying the spatial arrangement of the active and passive layers as well as the hinge joints. Several variations of the articulated building blocks are demonstrated in Fig. 2D, showing that the existence of the hinge joints can result in an entirely different form.

## Assembly and motion planning rules of the modular system

Considering the overall structural stiffness, freedom of assembly, and programmability of 4D micro-building blocks, we further introduce an octagonal prismatic microcylinder as the basic building blocks to construct a larger and more complicated morphing modular system that follows the superposition principle. From the side view in Fig. 3A, we can see that the octagonal prismatic building block consists of a pair of active layers and hinge joints as well as three pairs of passive layers. Its 3D configuration can be viewed as the extrusion of the side view in the normal direction. The deformation of a single prismatic building block is also simulated by FEA. The shrinkage of the building block generates a rotational movement in the assembled chain blocks, as shown in Fig. 3B. Each building block can be considered as a rotational joint connecting to another with a link (pillar). Assembling multiple building blocks resembles a robotic arm to generate desired 3D movements. The motion of assembled chains with a limited number of building blocks can also be well estimated by FEA, in good agreement with experimental results. However, FEA fails to capture the complex motion generated by the assembly of a large number ($n > 60$) of building blocks, as the numerical results tend to diverge. To address this issue, we introduce the DH parameters, which are used to calculate the shape transformations of a robotic arm composed of multiple joints and rigid bars. The DH parameters follow the superposition principle and describe any complex transformations with only four physical parameters in a closed analytical form (*48*, *49*). The kinematics equations for the series chain of a modular system are obtained using a transformation [$Z$] to characterize the relative movement allowed at each joint and a separate transformation [$X$] to define the dimensions of each link. The result is a sequence of transformations that alternate joint

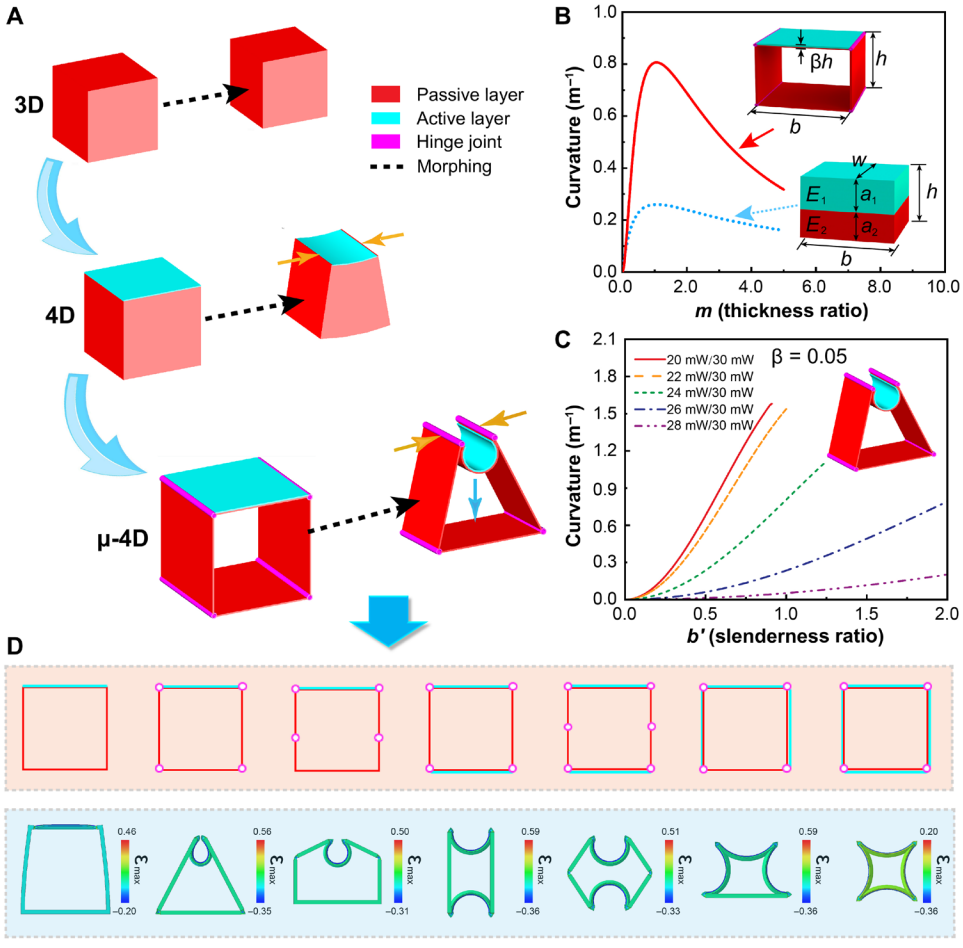


**Fig. 2. Evolution of 3D-printed building blocks.** (**A**) 4D micro-building blocks evolve from conventional static 3D-printed building blocks to deformable building blocks and further to articulated building blocks owing to the development of active materials and micromachining techniques. The shrinkage of the active layer mainly drives the deformation during decreasing of the solvent pH, which makes the bilayer structures bend toward the active layer. (**B**) Effect of the thickness ratio between the active layer and passive layer (*m*) on the bending curvature (κ), indicating that the articulated building blocks deform more than conventional bilayer building blocks. (**C**) Bending curvature of the articulated building blocks finely tuned by varying the slenderness ratio (*b*′) between the width and height of the blocks and the laser parameters between the active and passive layers. (**D**) Various simulated shape transformation modes of the articulated building blocks by varying the spatial arrangement of the bilayer mechanisms and the compliant hinge joints.

and link transformations from the base of the chain to its end link, which is equated to the specified position for the end link

$$[T] = [Z_1][X_1][Z_2][X_2]\cdots\ [Z_{n-1}][X_{n-1}] \quad (3)$$

where $T$ is the transformation locating the end link of the last building block. This convention positions the joint frame such that it consists of a screw displacement along the $Z$ axis

$$[Z_i] = \mathrm{Trans}_{z_i}(d_i)\,\mathrm{Rot}_{z_i}(\theta_{z_i}) \quad (4)$$

and it positions the link frame such that it consists of a screw displacement along the $X$ axis

$$[X_i] = \mathrm{Trans}_{x_i}(R_{i,i+1})\,\mathrm{Rot}_{x_i}(\alpha_{i,i+1}) \quad (5)$$

where $\theta_{zi}$, $d_i$, $R_i$, and $\alpha_{i,\,i+1}$ are known as the DH parameters (see section S4). These parameters can be implemented in our modular morphing system. They define the assembly and motion planning rules of the building blocks shown in Fig. 3 (B to E). Figure 3 (B and C) shows the simulated rotational movement of five assembled building blocks encoded with various $\theta_z$ and $R$. These building blocks are connected to each other with a rigid bar to avoid the interaction of deformations between each building block, ensuring the validity of the superposition principle. The amplitude and orientation of each building block rotating about the $Z$ axis are determined by ($\theta_{zi}$) and can be controlled by varying the laser power density and spatial arrangement of the internal active layers, respectively. Figure 3D shows each building block assembled with offsets ($d_i$) along the opposite Z axis. Therefore, Fig. 3, B and D, together represent the screw displacement along the $Z$ axis, resembling Eq. 4, while the other screw displacement along the $X$ axis is realized in the combination of Fig. 3, C and E. Figure 3C shows that connecting the rotational joints with inactive building blocks can expand the rotational radius ($R_{i,\,i+1}$) along the $X$ axis. Meanwhile, Fig. 3E shows building blocks assembled with angles ($\alpha_{i,\,i+1}$) rotating about the $X$ axis, measured from the previous $Z$ axis to the new $Z$ axis. These four parameters together determine the 3D transformation and assembly rules of the proposed modular systems.

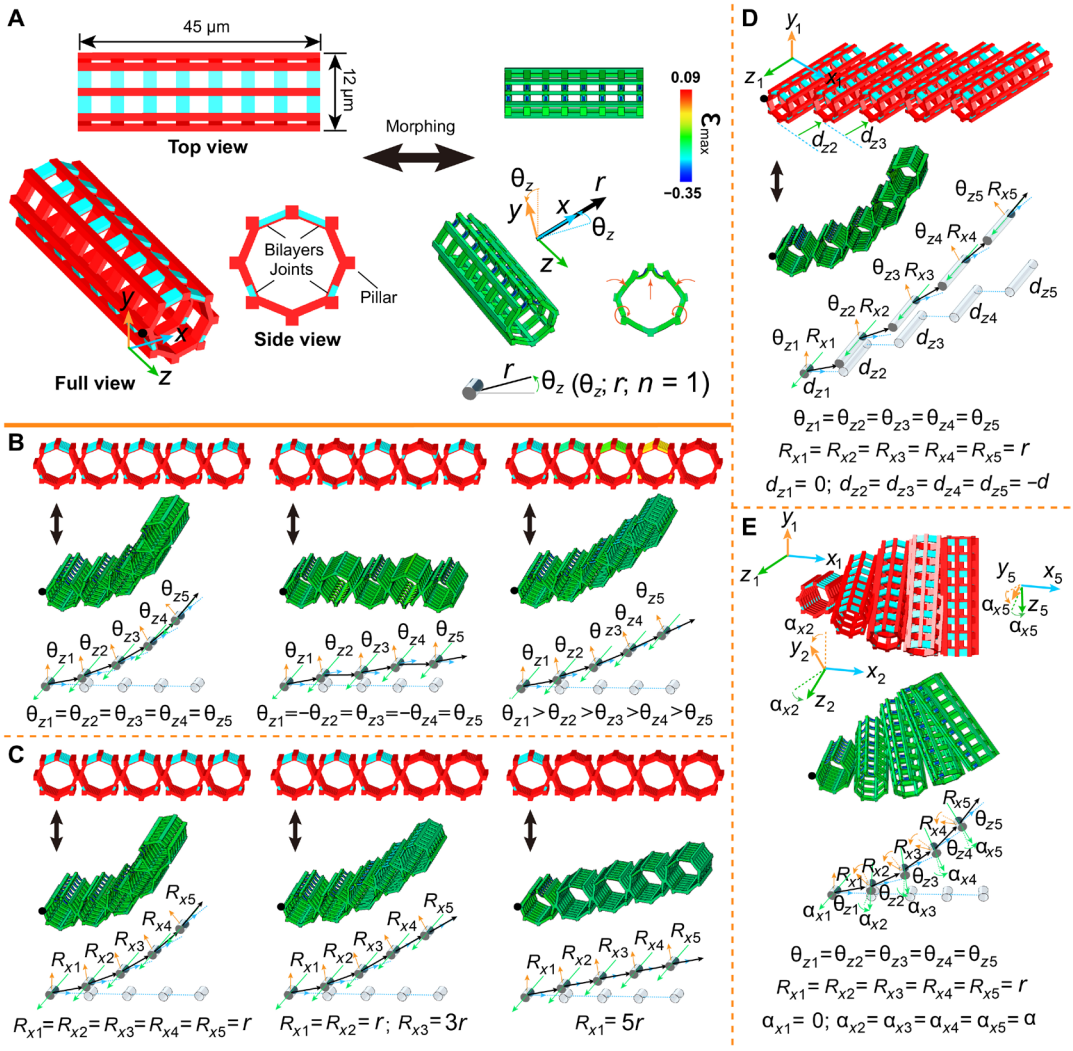


**Fig. 3. Design principle and assembly rules of the modular system with the aid of finite element simulations.** (**A**) Schematics and design geometry of the articulated building blocks whose basic structure is an octagonal prismatic hollow cylinder composed of pairs of active layers, passive layers, and hinge joints. (**B**) Rotational deformation induced by the shrinking of the active layers. Each building block can be viewed as a combination of a rotational joint and a rigid bar, resembling a robotic arm. (**C** to **E**) Schematics of rotational movements with controlled amplitude and orientation enabled by the assembly of various preprogrammed building blocks. (B), (C), (D), and (E) define how the four DH parameters θ, *R*, *d*, and α are implemented in our modular building blocks, respectively. FEA provides a means for the quantitative assembly of the complex modular system.

## Inverse and forward design of the modular systems

Given an arbitrary 3D shape as a target, we can convert it to a discrete counterpart composed of a finite number of joints. We can then obtain the DH parameters by inverse kinematics and construct the shape transformation between the target and initially assembled building blocks with Eq. 3 (see Fig. 4A, fig. S5, and section S4 for more details). For instance, consider a wave shape as a target shape and an initially assembled design with the shape of a roll. The DH parameters facilitate finding the transformation between the wave shape and the roll shape. Here, $\theta_z$ is the only variable parameter connecting the wave and roll, and we encode this parameter into the roll for it to morph from the roll shape into the wave shape. It is vital that the number of discretized joints of the target must be the same as the number of building blocks in the assembled structure. Figure 4B shows experimental results with geometrically identical planar stripes, which consist of 60 building blocks encoded with various $\theta_z$, *d*, and *R* that can transform into various target shapes, namely, honeycomb, roll, and wave [see Fig. 4B (I to III) and movies S1 to S6]. Their inverse parameters ($\theta_z$) are provided in tables S1 and S2.

Typically, an inverse design can be reversed to a forward design. However, in the case of goggles, the reverse of the inverse design is distinct from its forward design. Note that if a collision occurs in the path of the shape transformation, then the forward kinematics fail to capture the transformation. We show that the planar stripe composed of all building blocks encoded with the same $\theta_z$ can also transform into the shape of goggles, in which two circles with identical curvatures are created, without following the inverse design (Fig. 4B, IV). Figure 4B (V and VI) shows experimental results of the screw displacement along the *Z* axis with varying $d_i$ and $\theta_z$ in each building block, which can be captured by Eq. 4. By adding a constant *Z* axis offset ($d_i$) into the assembly, the goggles can be converted to a helix, and the roll shape becomes a spiral shape.

Using three parameters (*R*, *d*, and $\theta_z$), as shown in Fig. 4, we gain control over the forward and inverse problems of the relatively simple

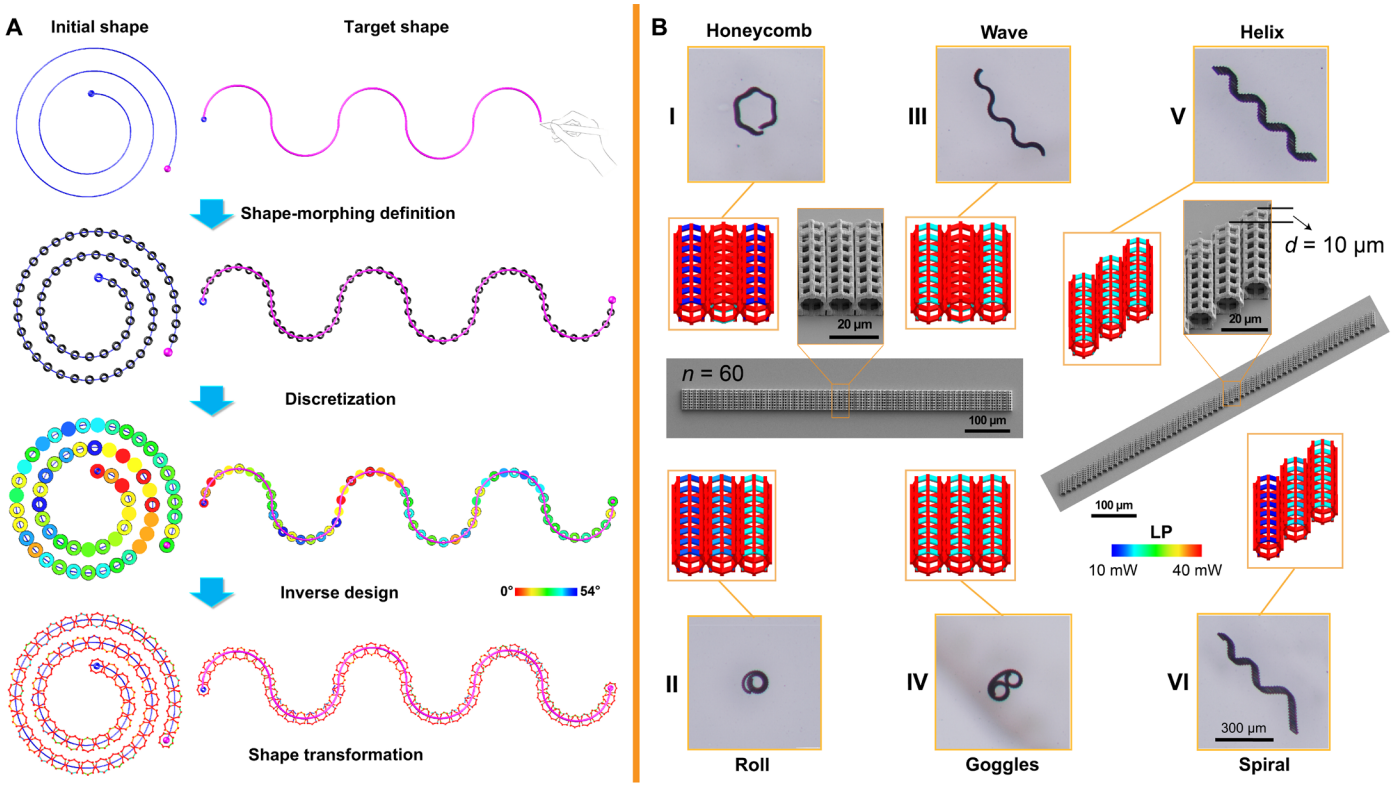


**Fig. 4. Inverse and forward design of morphing modular systems.** (**A**) Inverse problem finding for programming a structure that morphs into the desired shape. Given an arbitrary shape, such as a wave, the modular design converts it to a discrete counterpart with a finite number of joints and then obtains the DH parameters. The modular system subsequently constructs the shape transformation between the given wave shape and an assembled roll configuration by encoding the inversed $\theta_z$ into the roll, for it to morph into the shape of a wave. In the image of the inverse design of a roll encoded with different colors, the solid circles indicate that $\theta_z$ is positive, and the hollow circles indicate that $\theta_z$ is negative. (**B**) Optical images of the assembled building blocks encoded with different DH parameters.

modular structures (1D and 2D assembly and single rotational freedom). Furthermore, by assigning the fourth parameter α to enable 3D assembly, we can construct complex 3D structures encoded with more sophisticated 3D-to-3D shape transformations. Following the design principle of forward kinematics, provided in Fig. 3, we further devised a micrometer-scale transformer by the 3D assembly and 3D motion planning of 4D building blocks (Fig. 5A) and printed it using the 4D DLW (Fig. 5B). Five main functional parts including the neck (I), shoulder (II), arms (III), backbone (IV), and legs (V) are engineered, and their connections are described in Fig. 5C. Transformations of each compartment can be captured separately by a series of DH parameters, shown in Fig. 5D. We choose this transformer as a demonstration because it uses a combination of several unique transformations to realize its change in shape between a race car and a humanoid robot (Fig. 5E).

To the best of our knowledge, this is the first time a transformer has been created that automatically changes its shape and stands up at such a small scale (see movie S7). However, one of the major challenges when designing a transformer is to ensure that the transformation of each component occurs simultaneously. It is especially important to have a rational design such that each component does not interfere with the others to ensure the desired shape transformation. This is the reason why the microscale transformer shown in Fig. 5 looks oversimplified compared to its large-scale counterparts. Real 4D-printed structures, in which the time dimension can also be encoded during printing, would notably facilitate reconfigurable designs as various compartments that can transform sequentially in desired orders.

## CONCLUSION

We proposed a programmable modular design based on the assembly of 4D micro-building blocks to facilitate the complex forward and inverse problems of 4D printing. The modular design can reconstruct large and complex 3D structures, and their shape transformations with the 3D assembly of replicated 4D building blocks encoded with small and discretized deformations. Forward kinematics and the DH parameters are used to provide assembly guidelines and capture shape transformations. FEA predicts the shape evolution of each building block without taking the whole structure into account. This notably reduces the computational complexity. We demonstrated that a microscaled transformer capable of complex 3D shape transformations can be devised and fabricated by using the four DH parameters and single-step DLW fabrication in photoresponsive hydrogels. We expect that the proposed modular design, which resembles the forward and inverse kinematics of a robotic arm, will pave the way to facilitate the design of complex direct 4D printing.

## MATERIALS AND METHODS

### Synthesis of gel precursors

In a typical procedure, *N*-isopropylacrylamide (NIPAAm; 98%) and acrylic acid (AAc; 99%) served as the functional monomers of the stimuli-responsive gel and were added to an ethyl lactate (EL; 98%) solution and stirred vigorously for 30 min. Polyvinylpyrrolidone (PVP; average molecular weight, ~1,300,000) was added to adjust the photoresist viscosity to prevent structural collapse and shifting

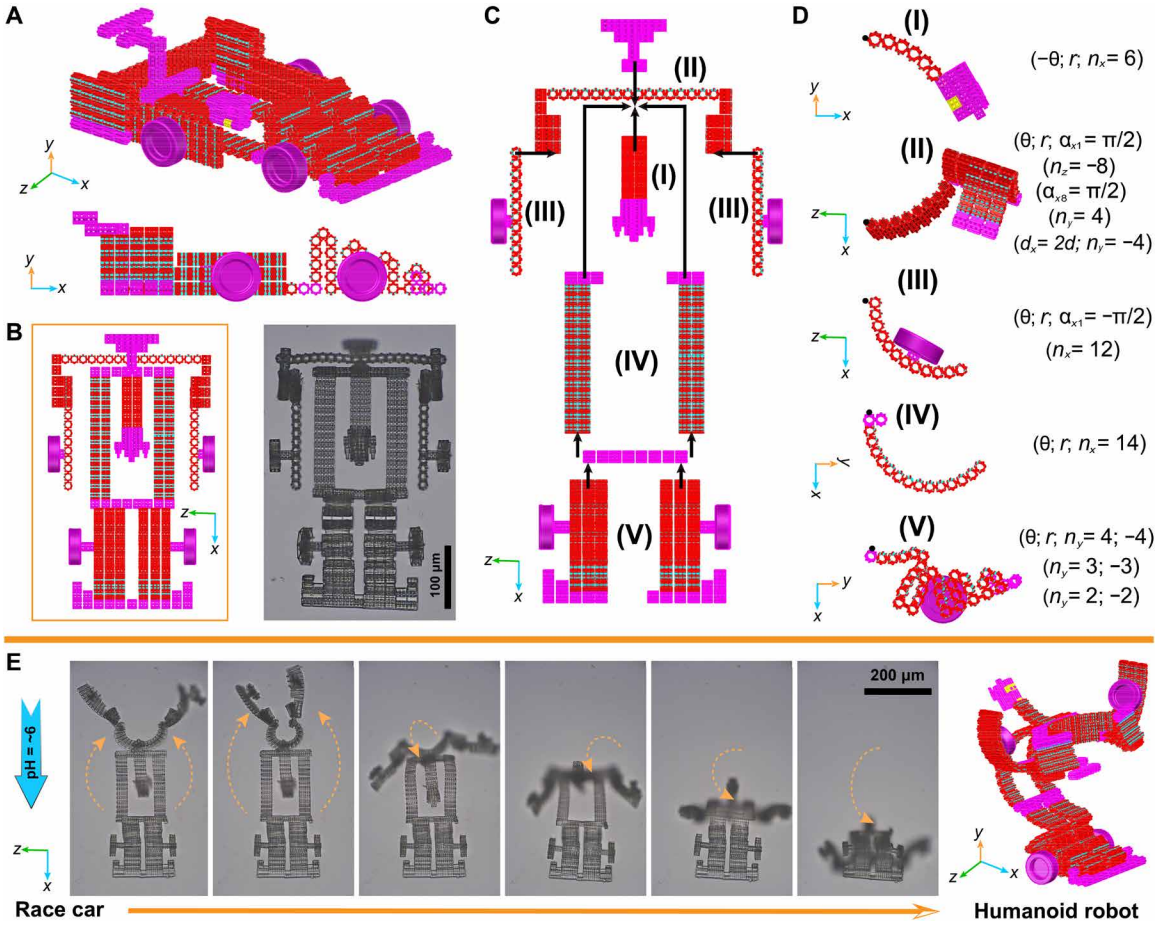


**Fig. 5. 3D assembly of 4D building blocks for constructing a micrometer-scale transformer.** (**A**) Computer-aided design model of a microscale race car following the proposed assembly rule. The color pink denotes the components that are rigid and nondeformable. (**B**) 4D DLW design and fabrication of the devised race car. (**C**) Detailed connections of the five main parts: neck, shoulder, arms, backbone, and legs. (**D**) Programmed deformation of each compartment encoded with defined DH parameters. (**E**) Sequential optical images showing the 3D-to-3D shape-morphing process of the microscale transformer from a race car to a humanoid robot. The blue arrow denotes the diffusion direction of acidic fluid flow.

during the construction of the complex 3D architectures. After complete dissolution, the above solution, dipentaerythritol pentaacrylate (DPEPA; 98%) cross-linker, triethanolamine (TEA; 99%) photosensitizer, and the 4,4′-bis (diethylamino) benzophenone (EMK; 97%)/*N*,*N*-dimethylformamide (DMF; 99.5%) photoinitiator solution (20 weight %) were mixed and stirred for 2 hours to obtain a homogeneous and transparent gel precursor. The photoresist was stored in an ambient ultraviolet light–free condition before use. NIPAAm, AAc, EL, PVP, DMF, and TEA were procured from Aladdin Chemicals. EMK was obtained from Reading Chemical Technology (Shanghai) Co. Ltd. DPEPA was provided by American Barki Chemical Inc. All chemicals were used without further purification.

### Procedures of 4D μ-printing

Before printing, the borosilicate glass square substrate (22 mm by 22 mm, 0.13 to 0.17 mm thick; Thermo Fisher Scientific Inc.) was cleaned with acetone, isopropyl alcohol (IPA), and deionized water and dried under nitrogen before being placed in a 120°C oven for 20 min. After cooling to room temperature, the surface was modified by using an oxygen plasma to provide the printed microstructure with good adhesion. A gel precursor was dropped onto the glass slide, in which the microstructure was printed with a commercially available 3D laser lithography system (Photonic Professional GT, Nanoscribe GmbH) with a 63× 1.4 numerical aperture (NA) oil-immersion objective. During the fabrication, the laser power (0 to 50 mW) with a 780-nm wavelength and scanning speed (0 to 100 mm/s) were programmed to cross-link the materials with various densities. After printing, the samples were developed with IPA for 30 min and rinsed with fresh IPA twice, followed by immersion in ultrapure water.

### FEA and computer-aided design

We carried out an FEA to simulate the response of 4D-printed microstructures to various stimuli, as mentioned in the main text. Briefly, we built 3D models of these microstructures and generated finite element meshes with element type C3D8H (eight-node linear brick, hybrid) by using the Abaqus software (Dassault Systèmes S.A., France) to perform the numerical simulation analysis. We used the theoretical model of Hong and co-workers (*47*) to characterize the deformation of gel materials in different chemical potential solvents, in which the parameters $Nv$ and $\chi$ were determined through the experimentally fitted data curves as shown in Fig. 1C. Practically, we introduced a user-defined subroutine of hyperelastic materials

(UHYPER) into Abaqus to specify the mechanical properties of gel-based microstructures under different exposure dosages and assumed that the dimensionless parameters represent a chemical potential of zero. In all numerical simulations, we ignored the influence of gravity because the gel density in the swollen state was very close to that of water or other solutions that we used in the experiments. Similarly, we performed an FEA-based computer-aided design to characterize morphological changes in microstructures before printing. By varying $\mu$, we can simulate the shape changes at various pH values. As mentioned before, we specified $\mu = 0$ when the printed structures are at the fully swollen state and pH $\approx$ 9. Comparing the FEA results with the experiments, we obtained that $\mu = -2$ when the printed structures are in an entirely shrinking state (in acid solvents with pH $\approx$ 6).

## SUPPLEMENTARY MATERIALS

Supplementary material for this article is available at http://advances.sciencemag.org/cgi/content/full/6/3/eaav8219/DC1

Section S1. Tests for swelling, shrinking, and mechanical properties of printed materials
Section S2. Theoretical modeling and parameter determination
Section S3. Deformation comparison between conventional and articulated building blocks
Section S4. Inverse design
Fig. S1. Characterization of swelling, shrinking, and mechanical properties of gel materials.
Fig. S2. Schematic curvatures of different 4D-printing strategies and geometrical sizes.
Fig. S3. Design concepts and deformation forms of two 4D-printing strategies.
Fig. S4. Comparison between experimental results of helical building blocks and the finite element simulation.
Fig. S5. Inverse design based on 4D micro-building blocks.
Table S1. Rotation angle parameters of the honeycomb-to-wave transformation.
Table S2. Rotation angle parameters of a spiral-to-wave transformation.
Movie S1. Modular morphing system consisting of 60 building blocks encoded into honeycomb shapes.
Movie S2. Modular morphing system consisting of 60 building blocks encoded into roll shapes.
Movie S3. Modular morphing system consisting of 60 building blocks encoded into wave shapes.
Movie S4. Modular morphing system consisting of 60 building blocks encoded into goggle shapes.
Movie S5. Modular morphing system consisting of 60 building blocks encoded into helix shapes.
Movie S6. Modular morphing system consisting of 60 building blocks encoded into spiral shapes.
Movie S7. Transformer assembled by 4D micro-building blocks.
References (*50*–*52*)

## REFERENCES AND NOTES


1. J. H. Pikul, S. Li, H. Bai, R. T. Hanlon, I. Cohen, R. F. Shepherd, Stretchable surfaces with programmable 3D texture morphing for synthetic camouflaging skins. *Science* **358**, 210–214 (2017).
2. M. Schaffner, J. A. Faber, L. Pianegonda, P. A. Rühs, F. Coulter, A. R. Studart, 3D printing of robotic soft actuators with programmable bioinspired architectures. *Nat. Commun.* **9**, 878 (2018).
3. E. W. Hawkes, L. H. Blumenschein, J. D. Greer, A. M. Okamura, A soft robot that navigates its environment through growth. *Sci. Robot.* **2**, eaan3028 (2017).
4. B. Shin, J. Ha, M. Lee, K. Park, G. H. Park, T. H. Choi, K.-J. Cho, H.-Y. Kim, Hygrobot: A self-locomotive ratcheted actuator powered by environmental humidity. *Sci. Robot.* **3**, eaar2629 (2018).
5. H.-W. Huang, M. W. Tibbitt, T.-Y. Huang, B. J. Nelson, Matryoshka-inspired micro-origami capsules to enhance loading, encapsulation, and transport of drugs. *Soft Robot.* **6**, 150–159 (2019).
6. A. Lamoureux, K. Lee, M. Shlian, S. R. Forrest, M. Shtein, Dynamic kirigami structures for integrated solar tracking. *Nat. Commun.* **6**, 8092 (2015).
7. B. J. Nelson, I. K. Kaliakatsos, J. J. Abbott, Microrobots for minimally invasive medicine. *Annu. Rev. Biomed. Eng.* **12**, 55–85 (2010).
8. E. Gultepe, J. S. Randhawa, S. Kadam, S. Yamanaka, F. M. Selaru, E. J. Shin, A. N. Kalloo, D. H. Gracias, Biopsy with thermally-responsive untethered microtools. *Adv. Mater.* **25**, 514–519 (2013).
9. M. Cianchetti, C. Laschi, A. Menciassi, P. Dario, Biomedical applications of soft robotics. *Nat. Rev. Mater.* **3**, 143–153 (2018).
10. S. Fusco, M. S. Sakar, S. Kennedy, C. Peters, R. Bottani, F. Starsich, A. Mao, G. A. Sotiriou, S. Pané, S. E. Pratsinis, D. Mooney, B. J. Nelson, An integrated microrobotic platform for on-demand, targeted therapeutic interventions. *Adv. Mater.* **26**, 952–957 (2014).
11. S. Li, Q. Jiang, S. Liu, Y. Zhang, Y. Tian, C. Song, J. Wang, Y. Zou, G. J. Anderson, J.-Y. Han, Y. Chang, Y. Liu, C. Zhang, L. Chen, G. Zhou, G. Nie, H. Yan, B. Ding, Y. Zhao, A DNA nanorobot functions as a cancer therapeutic in response to a molecular trigger in vivo. *Nat. Biotechnol.* **36**, 258–264 (2018).
12. E. Hawkes, B. An, N. M. Benbernou, H. Tanaka, S. Kim, E. D. Demaine, D. Rus, R. J. Wood, Programmable matter by folding. *Proc. Natl. Acad. Sci. U.S.A.* **107**, 12441–12445 (2010).
13. Z. Yan, F. Zhang, J. Wang, F. Liu, X. Guo, K. Nan, Q. Lin, M. Gao, D. Xiao, Y. Shi, Controlled mechanical buckling for origami-inspired construction of 3D microstructures in advanced materials. *Adv. Funct. Mater.* **26**, 2629–2639 (2016).
14. S. Felton, M. Tolley, E. Demaine, D. Rus, R. Wood, A method for building self-folding machines. *Science* **345**, 644–646 (2014).
15. R. M. Erb, J. S. Sander, R. Grisch, A. R. Studart, Self-shaping composites with programmable bioinspired microstructures. *Nat. Commun.* **4**, 1712 (2013).
16. S. Armon, E. Efrati, R. Kupferman, E. Sharon, Geometry and mechanics in the opening of chiral seed pods. *Science* **333**, 1726–1730 (2011).
17. S. Xu, Z. Yan, K.-I. Jang, W. Huang, H. Fu, J. Kim, Z. Wei, M. Flavin, J. McCracken, R. Wang, A. Badea, Y. Liu, D. Xiao, G. Zhou, J. Lee, H. U. Chung, H. Cheng, W. Ren, A. Banks, X. Li, U. Paik, R. G. Nuzzo, Y. Huang, Y. Zhang, J. A. Rogers, Assembly of micro/nanomaterials into complex, three-dimensional architectures by compressive buckling. *Science* **347**, 154–159 (2015).
18. R. M. Erb, R. Libanori, N. Rothfuchs, A. R. Studart, Composites reinforced in three dimensions by using low magnetic fields. *Science* **335**, 199–204 (2012).
19. H. Aharoni, Y. Xia, X. Zhang, R. D. Kamien, S. Yang, Universal inverse design of surfaces with thin nematic elastomer sheets. *Proc. Natl. Acad. Sci. U.S.A.* **115**, 7206–7211 (2018).
20. A. S. Gladman, E. A. Matsumoto, R. G. Nuzzo, L. Mahadevan, J. A. Lewis, Biomimetic 4D printing. *Nat. Mater.* **15**, 413–418 (2016).
21. J. Kim, S. E. Chung, S.-E. Choi, H. Lee, J. Kim, S. Kwon, Programming magnetic anisotropy in polymeric microactuators. *Nat. Mater.* **10**, 747–752 (2011).
22. H.-W. Huang, M. S. Sakar, A. J. Petruska, S. Pané, B. J. Nelson, Soft micromachines with programmable motility and morphology. *Nat. Commun.* **7**, 12263 (2016).
23. W. Hu, G. Z. Lum, M. Mastrangeli, M. Sitti, Small-scale soft-bodied robot with multimodal locomotion. *Nature* **554**, 81–85 (2018).
24. J. Kim, J. A. Hanna, M. Byun, C. D. Santangelo, R. C. Hayward, Designing responsive buckled surfaces by halftone gel lithography. *Science* **335**, 1201–1205 (2012).
25. Z. Ding, C. Yuan, X. Peng, T. Wang, H. J. Qi, M. L. Dunn, Direct 4D printing via active composite materials. *Sci. Adv.* **3**, e1602890 (2017).
26. Y. Kim, H. Yuk, R. Zhao, S. A. Chester, X. Zhao, Printing ferromagnetic domains for untethered fast-transforming soft materials. *Nature* **558**, 274–279 (2018).
27. G. Z. Lum, Z. Ye, X. Dong, H. Marvi, O. Erin, W. Hu, M. Sitti, Shape-programmable magnetic soft matter. *Proc. Natl. Acad. Sci. U.S.A.* **113**, E6007–E6015 (2016).
28. D. Rus, M. T. Tolley, Design, fabrication and control of origami robots. *Nat. Rev. Mater.* **3**, 101–112 (2018).
29. H.-W. Huang, T.-Y. Huang, M. Charilaou, S. Lyttle, Q. Zhang, S. Pané, B. J. Nelson, Investigation of magnetotaxis of reconfigurable micro-origami swimmers with competitive and cooperative anisotropy. *Adv. Funct. Mater.* **28**, 1802110 (2018).
30. D. Kokkinis, M. Schaffner, A. R. Studart, Multimaterial magnetically assisted 3D printing of composite materials. *Nat. Commun.* **6**, 8643 (2015).
31. T. J. Wallin, J. Pikul, R. F. Shepherd, 3D printing of soft robotic systems. *Nat. Rev. Mater.* **3**, 84–100 (2018).
32. L.-K. Ma, Y. Zhang, Y. Liu, K. Zhou, X. Tong, Computational design and fabrication of soft pneumatic objects with desired deformations. *ACM Trans. Graph.* **36**, 239 (2017).
33. T.-Y. Huang, M. S. Sakar, A. Mao, A. J. Petruska, F. Qiu, X.-B. Chen, S. Kennedy, D. Mooney, B. J. Nelson, 3D printed microtransporters: Compound micromachines for spatiotemporally controlled delivery of therapeutic agents. *Adv. Mater.* **27**, 6644–6650 (2015).
34. J. A. Faber, A. F. Arrieta, A. R. Studart, Bioinspired spring origami. *Science* **359**, 1386–1391 (2018).
35. M. Wehner, R. L. Truby, D. J. Fitzgerald, B. Mosadegh, G. M. Whitesides, J. A. Lewis, R. J. Wood, An integrated design and fabrication strategy for entirely soft, autonomous robots. *Nature* **536**, 451–455 (2016).
36. R. L. Truby, J. A. Lewis, Printing soft matter in three dimensions. *Nature* **540**, 371–378 (2016).
37. Z. Ding, O. Weeger, H. J. Qi, M. L. Dunn, 4D rods: 3D structures via programmable 1D composite rods. *Mater. Des.* **137**, 256–265 (2018).
38. F. Momeni, S. M. Mehdi Hassani.N, X. Liu, J. Ni, A review of 4D printing. *Mater. Des.* **122**, 42–79 (2017).
39. H. Fu, K. Nan, W. Bai, W. Huang, K. Bai, L. Lu, C. Zhou, Y. Liu, F. Liu, J. Wang, M. Han, Z. Yan, H. Luan, Y. Zhang, Y. Zhang, J. Zhao, X. Cheng, M. Li, J. W. Lee, Y. Liu, D. Fang, X. Li, Y. Huang, Y. Zhang, J. A. Rogers, Morphable 3D mesostructures and microelectronic devices by multistable buckling mechanics. *Nat. Mater.* **17**, 268–276 (2018).
40. H. Lee, J. Zhang, H. Jiang, N. X. Fang, Prescribed pattern transformation in swelling gel tubes by elastic instability. *Phys. Rev. Lett.* **108**, 214304 (2012).

41. J. Seo, J. Paik, M. Yim, Modular reconfigurable robotics. *Annu. Rev. Control Robot. Auton. Syst.* **2**, 63–88 (2019).
42. E. Yoshida, S. Murata, A. Kamimura, K. Tomita, H. Kurokawa, S. Kokaji, A self-reconfigurable modular robot: Reconfiguration planning and experiments. *Int. J. Robot. Res.* **21**, 903–915 (2002).
43. M. Yim, W.-m. Shen, B. Salemi, D. Rus, M. Moll, H. Lipson, E. Klavins, G. S. Chirikjian, Modular self-reconfigurable robot systems [grand challenges of robotics]. *IEEE Robot. Autom. Mag.* **14**, 43–52 (2007).
44. M. Yao, C. H. Belke, H. Cui, J. Paik, A reconfiguration strategy for modular robots using origami folding. *Int. J. Robot. Res.* **38**, 73–89 (2019).
45. K. C. Cheung, N. Gershenfeld, Reversibly assembled cellular composite materials. *Science* **341**, 1219–1221 (2013).
46. D. Jin, Q. Chen, T.-Y. Huang, J. Huang, L. Zhang, H. Duan, Four-dimensional direct laser writing of reconfigurable compound micromachines. *Mater. Today*, https://doi.org/10.1016/j.mattod.2019.06.002 (2019).
47. W. Hong, Z. Liu, Z. Suo, Inhomogeneous swelling of a gel in equilibrium with a solvent and mechanical load. *Int. J. Solids Struct.* **46**, 3282–3289 (2009).
48. J. Denavit, R. S. Hartenberg, A kinematic notation for lower-pair mechanisms based on matrices. *ASME J. Appl. Mech.* **77**, 215–221 (1955).
49. R. Hartenberg, J. Denavit, *Kinematic Synthesis of Linkages* (McGraw-Hill Series in Mechanical Engineering, McGraw-Hill, 1964).
50. S. Cai, Z. Suo, Mechanics and chemical thermodynamics of phase transition in temperature-sensitive hydrogels. *J. Mech. Phys. Solids* **59**, 2259–2278 (2011).
51. Z. Liu, W. Toh, T. Y. Ng, Advances in mechanics of soft materials: A review of large deformation behavior of hydrogels. *Int. J. Appl. Mech.* **07**, 1530001 (2015).
52. B. Y. S. Timoshenko, Analysis of bi-metal thermostats. *J. Opt. Soc. Am.* **11**, 233–255 (1925).

**Acknowledgments:** We thank Q.W. Chao and S.N. Lv for their insightful comments and suggestions for editing this paper. We also thank W. Cui from Nanoscribe GmbH (China) and F. Qiu from FemtoTools AG for technical support. **Funding:** This work was supported financially by the National Natural Science Foundation of China under grant nos. 91848201, 11988102, 11521202, 11702003, 11802004, and 11872004; by the Beijing Natural Science Foundation under grant no. L172002; and by the Hong Kong Research Grants Council (RGC) under grant no. JLFS/E-402/18. **Author contributions:** T.-Y.H., H.-W.H., and H.L.D. conceived the idea and designed the research. T.-Y.H. and H.L.D. constructed the experimental platform. T.-Y.H., D.D.J., and Q.Y.C. developed the 4D μ-printing based on direct laser writing. T.-Y.H., H.-W.H., Q.Y.C., D.D.J., and L.Z. performed the research and analyzed the data. Q.Y.C. and J.Y.H. formulated and implemented the computational model. H.-W.H., T.-Y.H., and H.L.D. wrote the paper with contributions from all authors. **Competing interests:** T.-Y.H., H.L.D., and D.D.J. are inventors on a patent application related to this work filed by Peking University (CN201810153284.6, filed 14 February 2018). T.-Y.H. and H.L.D. are inventors on a patent related to this work filed by Peking University (201810151527.2, filed 14 February 2018). The authors declare no other conflict of interest. **Data and materials availability**: All data needed to evaluate the conclusions in the paper are present in the paper and/or the Supplementary Materials. Additional data related to this paper may be requested from the authors.

Submitted 23 October 2018
Accepted 20 November 2019
Published 17 January 2020
10.1126/sciadv.aav8219

**Citation:** T.-Y. Huang, H.-W. Huang, D. D. Jin, Q. Y. Chen, J. Y. Huang, L. Zhang, H. L. Duan, Four-dimensional micro-building blocks. *Sci. Adv.* **6**, eaav8219 (2020).